Numerical modeling of a benchmark experiment on equiaxed solidification of a Sn–Pb alloy with electromagnetic stirring and natural convection

Tao Wang, Lakhdar Hachani, Yves Fautrelle, Yves Delannoy, Engang Wang, Xiaodong Wang, Olga Budenkova

To cite this version:

Tao Wang, Lakhdar Hachani, Yves Fautrelle, Yves Delannoy, Engang Wang, et al.. Numerical modeling of a benchmark experiment on equiaxed solidification of a Sn–Pb alloy with electromagnetic stirring and natural convection. International Journal of Heat and Mass Transfer, 2020, 151, pp.119414. 10.1016/j.ijheatmasstransfer.2020.119414 . hal-03016901

HAL Id: hal-03016901
https://hal.science/hal-03016901v1

Submitted on 20 Nov 2020

Numerical Modeling of a Benchmark Experiment on Equiaxed Solidification of a Sn-Pb alloy with Electromagnetic Stirring and Natural Convection

Tao WANG[a,b,c], Lakhdar HACHANI[d], Yves FAUTRELLE[b], Yves DELANNOY[b], Engang WANG[a], Xiaodong WANG[e], Olga BUDENKOVA[b,*]

[a]*Key Laboratory of Electromagnetic Processing of Materials (Ministry of Education), Northeastern University, No. 3-11, Wenhua Road, Shenyang 110004, P. R. China*
[b]*Univ. Grenoble Alpes, CNRS, Grenoble INP, SIMAP, F-38000 Grenoble, France*
[c]*School of Metallurgy, Northeastern University, Shenyang 110004, P. R. China*
[d]*Laboratoire de physique des matériaux, Université Amar TelidjiLaghouat, Route de Ghardaia BP 37G, Laghouat, Algeria*
[e]*College of Material Science and Opto-electronic Technology, University of Chinese Academic Sciences, Beijing 100049, China*

Abstract

A three-phase volume averaged equiaxed model is applied to simulation of an experiment on solidification of the binary alloy Sn-10wt% Pb subjected to the electromagnetic stirring. The experiment, whose description was published earlier, was performed in a parallelepiped cavity under controlled cooling conditions and with real-time two-dimensional temperature measurement over a lateral surface of the cavity co-planar with direction of solidification. Applied numerical model treats motion of the liquid and equiaxed grains whose growth kinetics is taken into account and uses a double time step scheme to accelerate solution. Growth of columnar dendrite is not considered. It is shown that electromagnetic force acting in a direction opposite to the natural convection flow creates moderately turbulent flow in pure liquid which is treated with a realizable $k_\varepsilon - \varepsilon$ model. It is demonstrated that calculated temperature distribution in the cavity well reproduces temperature maps reconstructed from thermocouples measurements throughout the experiment. Final macrosegregation map and distribution of density grain number are qualitatively similar to those obtained in the exper-

---

[*]Corresponding author
Email address: `olga.budenkova@simap.grenoble-inp.fr` (Olga BUDENKOVA)

iment. Variation of intensity of electromagnetic stirring in numerical model shows that this affects shape and localization of positive segregation region at the bottom of the cavity.

Keywords: Solidification, Equiaxed model, Macrosegregation, Multiphase flows, Electromagnetic stirring, Natural convection, Numerical Modeling

---

1. Introduction

Macrosegregation defects often appear in alloys ingots during a long-time solidification and are mainly caused by fluid flow in a mushy zone and grains settling/floating [1, 2]. Heat treatment or rolling process which follows solidification, usually cannot eliminate these defects because diffusion process is slow while zones of macrosegregation can be large. This means that formation of such defects should be avoided during solidification process and it is believed that this can be realized via the control of liquid phase motion. Rather often, electromagnetic fields are used with an idea to implement such control and to affect solute distribution and grain structure [3, 4, 5, 6]. In particular, rotating and travelling magnetic fields are used to create electromagnetic force which may stir the bulk liquid. Experimentally, it was observed that electromagnetic stirring (EMS) can enhance heat dissipation in the melt [7], increase quantity of nuclei [8], promote columnar-to-equiaxed transition (CET) [9, 10, 11] and reduce macrosegregation [12]. Yet, it was also found that strengthened convective flow being structured can provoke even heavier macrosegregation. In laboratory-scale experiments a so-called “fishbone” segregation pattern was observed in solidification under rotating magnetic field [13, 14] and promotion of channel formation inside columnar mushy zone with use of travelling magnetic field [15]. In industrial continuous casting, for instance, formation of a centerline defect [16] or a so-called white band [17] were found. One may conclude that although use of EMS seems to be promising for prevention of macrosegregation, its application is still mainly based on trial and error method and may lead to unexpected results. It could be expected that numerical modelling can help to understand complex overlapping phenomena that occur during solidification with electromagnetic stirring and predict final segregation patterns and microstructure of the samples. Indeed, it was found that numerical models based on approximation of slurry or porous media were capable to reproduce characteristic segregation patterns observed in industrial solidification processes if equiaxed growth occurs in the sample [16, 18]. Alternatively, cellular automaton method successfully predicts the grains morphology and CET phenomenon based on distribution of constitutional undercooling [19, 20]. Yet, aforementioned numerical methods treat complex solidification process only in part, for instance, none of them takes into account effects related to grains transport which may be crucial for other solidification conditions or other modes of electromagnetic stirring. Furthermore, it should be noted that in most cases electromagnetic stirring makes bulk flow turbulent. Although serious experimental and theoretical efforts were made in order to understand effect of convection on solidification phenomena, this was not really extended for turbulent flows. First, this is related to the absence of experimental data. Second, a new formalism would be necessary to describe solid-liquid phase transition in turbulent flows. Indeed, governing equations for macroscopic solidification models are usually thought of as microscopic equations averaged over a representative volume which contains different types of solid structures with surrounding liquid. Yet, usual approach for turbulent theory, based on Reynolds averaging of Navier-Stokes equations assumes time-averaging procedure of instantaneous velocity field thus providing transport equations for mean flow as well for mean values of temperature and concentration and enhancement of diffusive transport due to velocity fluctuations. Consecutive application of these two averaging procedures to initial system of instantaneous microscopic equations is not evident because transport phenomena at microscale cannot be treated separately of velocity fluctuation at short time period, i.e. two averaging procedures actually could not be perform independently. In a more rigorous way, both procedures could be replaced with a unique ensemble statistical averaging, nevertheless, final equations would also contain terms related to combinations of microscale and short-time phenomena, for which closure relations are required [21, 22, 23]. Generally, experiments serve for finding the latter either due to in-situ observations or via indirect measurement.

Therefore, extensive experimental studies dedicated to the application of electromagnetic stirring in solidification and supported with numerical modeling are required. Yet, implementation of such experiment at industrial scale is hardly possible. Moreover, even at laboratory scale only few experiments with electromagnetic stirring provide information sufficient for implementation of boundary conditions into numerical model and data for further comparison of experimental and calculated results. Regarding in-situ observations, the work [15] already cited above deals with columnar growth under electromagnetic stirring. One can cite MICAST project, in which Al-based alloys are subjected to directional solidification in microgravity or in terrestrial conditions without and with electromagnetic stirring accompanied with some temperature measurements along the crucible [24]. In MICAST samples equiaxed structure prevails once electromagnetic stirring is activated. Another experimental set-up presented below and referred hereafter as AFRODITE is a solidification benchmark whose main feature is a real-time whole-field temperature measurement. The first experiment with this set-up was performed with a pure tin [25], then effect of different initial concentrations in solidification of Sn-Pb alloys was studied [26]. Samples of Sn-Pb alloy solidified under natural convection demonstrated mainly columnar structure with a small amount of equiaxed grains formed in a zone which solidified the latest. Several pronounced channels enriched with solute always appeared in the samples near the colder side. These experiments served for development and validation of numerical models [27, 28, 29]. The latest results obtained with the AFRODITE set-up were related to studies of various modes of EMS during solidification of a Sn-Pb alloy [30]. In particular, it was found that for the case with the Lorentz force acting in a direction opposite to the flow caused by gravity structure of the sample consisted mainly of equiaxed grains whose size varied slightly over the sample.

In this paper, we present three-dimensional numerical modeling of the experiment on solidification of Sn-10wt% Pb alloy with electromagnetic stirring which was performed in the AFRODITE set-up [30, 31]. Effect of EMS on solidification process is analyzed using a recently developed 3-phase equiaxed solidification model that accounts for the growth of equiaxed grains, their motion and formation of the macrosegregation [32]. Special attention is given to the treatment of the grains' packing, yet, dendrite fragmentation is not considered. It is demonstrated that in the experimental case a moderate turbulent flow develops in the bulk liquid, yet a general treatment of turbulence applied "ad-hoc" allows us to obtain final macrosegregation pattern similar to the one observed in the experiment. In order to understand the role of EMS, calculations are performed with different intensity of the Lorentz force.

2. Experimental procedure in the AFRODITE set-up

In the AFRODITE set-up solidification is performed in a parallelepiped cavity with inner size of 100 mm×60 mm×10 mm equipped with a lattice of 50 thermocouples over one of its largest faces (Fig.1(a)). The thermocouples are soldered into the cavity's wall such that they almost touch the melt and their measurements allow one to follow evolution of temperature field during solidification process. Two independent heat exchangers are put in contact with lateral left and right sides of the cavity, and combine resistive heating and water cooling. Each exchanger is equipped with 9 thermocouples and a feed-back control is implemented to govern cooling conditions. Other sides of the cavity may be considered as adiabatic due to special precautions taken to reduce convective and radiative heat exchange with the environment [33]. At the beginning of the experiment, a solid sample is placed in the cavity where it is melted, then overheated and kept at a uniform temperature for some time during which an electromagnetic stirring is applied to homogenize the liquid. After that an initial temperature distribution is imposed in the cavity via regulation of temperatures on the left and right heat exchangers. Most of experiments (with and without EMS) were performed with a difference of 40 degrees between the heat exchangers, yet, as explained below, temperature difference across the solidifying volume might be smaller. Finally, solidification is performed with cooling of the lateral sides of the cavity. Temperature variation at the heat exchangers during experiment is schematically shown in Fig. 1(b). To introduce the electromagnetic force, a travelling magnetic field is created with a flat coil placed horizontally below the cavity. In such configuration, the Lorentz force acts in the liquid mostly along the bottom and decreases exponentially in the vertical direction, an analytical expression for it is given below in the section 2.2. Direction of the Lorentz force depends on the polarity of the electric potential applied to the coil.

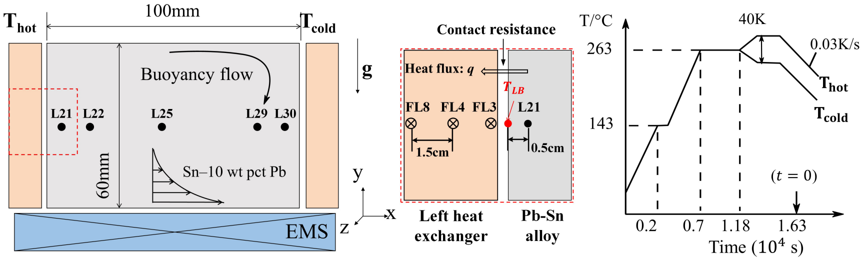

(a) (b)

Figure 1: Sketch of the AFRODITE set-up with indication of position of some thermocouples: L21 at $x = 5mm$, L22 at $x = 15mm$, L25 at $x = 45mm$, L29 at $x = 85mm$ and L30 at $x = 95mm$ all at the same height $y = 30mm$ and the contact resistance between the heat exchanger and solidifying volume (a), programmed temperature evolution at heat exchangers during the whole experiment with indication of the starting time for numerical simulations (b)

In the present work, we deal with solidification of a binary Sn-10wt%Pb alloy with the aimed cooling rate of 0.03 K/s. More details about the experiment and related results can been found in [30] for the experimental case referred there as a case number 3. Properties of the alloy and values for some other physical parameters are given in the Table 1.

2.1. Treatment of experimental boundary conditions

It should be underlined that in the experiment temperature distribution prior the solidification as well as cooling rate during solidification are programmed and controlled via temperature measurements at the heat exchangers. As discussed elsewhere [31, 29], a contact resistance may exist between the wall and the bulk and be dependent on the wettability of the walls by melt, on motion of liquid and on distribution of liquid fraction in the volume because of shrinkage during solidification. That means that actual temperature difference across the bulk should be smaller compared to that imposed on the heat exchangers and vary with transition from liquid to solid state. Furthermore the lateral cooling rate in the experiment can deviate from programmed one if intense solidification accompanied by a large amount of heat release occurs or if the water cooling is not sufficient. To take these effects into account, temperature at the inner side of the lateral walls is recalculated using temperature measurement made by the thermocouples placed on the heat exchangers and those on the frontal side of the cavity near their lateral sides. According to the scheme in Fig.1(a), if convective heat transfer is neglected near the lateral wall, the heat flux should conserve along the horizontal axis x. Using a finite difference discretization, this condition for the left side of the cavity can be written as [31]:

$$\kappa_H \left(1.5T_{FL3} - 2T_{FL4} + 0.5T_{FL8}\right)/\Delta x_{H,T} = \kappa_S(T_{LB} - T_{L21})/(x_{L21} - x_{FL3}) \tag{1}$$

where $\kappa_H = 401\mathrm{W/(m{\cdot}K)}$ and $\kappa_S = 55\mathrm{W/(m{\cdot}K)}$ are the thermal conductivities of the heat exchanger (made of copper) and the sample respectively, $\Delta x_{H,T} = 1.5\mathrm{cm}$ is the distance between the thermocouples at the heat exchanger and T_{LB} is the temperature at the inner side of the left boundary. Other variables represent temperature values at the thermocouples given with their numbers and position in Fig. 1(a). Consequently, the value of T_{LB} (T_{RB} for the right side) can be found using values of temperature measured by neighboring thermocouples. Thus calculated temperature can be used as uniform Dirichlet boundary condition at the inner surface of the lateral side of the cavity. Yet, it could be appropriate to interpolate calculated variations T_{LB} and T_{RB} in time using analytical expressions as it was done in the present paper.

2.2. Travelling magnetic field in the AFRODITE set-up

A flat coil (similar to a linear motor) which was placed beneath the cavity to create stirring of the liquid was alimented with a 3-phase AC current with a frequency $f = 50$ Hz and nominal current 8.2 Ampers. Analytical solution of a two-dimensional problem of penetration of electromagnetic field in a narrow cavity performed in [34] provides the following expression for the effective Lorentz force acting inside a media with electrical conductivity σ:

$$F_{emf} = C_E \pi f \sigma k^* A_E^2 exp(-2k^* y) \tag{2}$$

where C_E is adjustable parameter accounting for the finite size of the coil, wave vector k^* takes into account the narrowness of the crucible and a so-called pole pitch of the coil, and A_E corresponds to the amplitude of the potential vector at the inner surface of the bottom side of the cavity. Among these three parameters only k^* can be defined analytically, yet for the case under consideration the value $k^* = 65\text{m}^{-1}$ was recommended in [31] contrary to the value 314m^{-1} derived in [34]. Recommended values for A_E and C_E were also different between [31] and [34] although at significantly less extent. In the present work we accepted an expression

$$F_x = A_{emf} exp(-2k^* y) \tag{3}$$

with values $k^* = 65\text{m}^{-1}$ and A_{emf} in the range $110-180$ N/m^3 that corresponds to $A_E = 1 \cdot 10^{-3}$ T·m and variation of C_E between $0.35 - 0.6$. This choice was made based on the comparison of the flow field obtained in simulations and ultrasound measurements of velocity presented in [31]. It should be noted that equation (3) neglects variation of the electromagnetic force along x direction which can have secondary effect of the flow, especially near walls of the cavity.

Table 1: Phase diagram, material properties and calculation parameters

	Symbol	**Units**	**Value**	**Ref.**
Phase diagram for Sn-Pb				
Melting temperature of pure Sn	T_{Sn}	K	505	
Eutectic temperature	T_{eut}	K	456	
Liquidus slope	m	$\mathrm{K\,wt\%^{-1}}$	-1.286	[35]
Partition coefficient	k		0.0656	[35]
Nominal concentration of Pb	c_0	wt%	10	
Physical properties				
Reference density(liquid)	ρ_{ref}	$\mathrm{kg\,m^{-3}}$	7246	[36]
Density	$\rho_l,\ \rho_s$	$\mathrm{kg\,m^{-3}}$	7246	[36]
Reference temperature	T^b_{ref}	K	510.15	
Thermal expansion coefficient	β_T	$\mathrm{K^{-1}}$	6.0×10^{-5}	[36]
Solutal expansion coefficient	β_c	$\mathrm{wt\%^{-1}}$	5.3×10^{-3}	[36]
Density of solid phase in buoyancy term	ρ^b_s	$\mathrm{kg\,m^{-3}}$	7199	[36]
Thermal conductivity	κ_l, κ_s	$\mathrm{W\,m^{-1}K^{-1}}$	55.0	[35]
Latent heat	L	$\mathrm{J\,kg^{-1}}$	61000	[35]
Specific heat	$c^l_p,\ c^s_p$	$\mathrm{J\,kg^{-1}K^{-1}}$	260	[35]
Diffusion coefficient for liquid	D_l	$\mathrm{m^2s^{-1}}$	10^{-8}	[35]
Dynamic viscosity for liquid	μ_l	Pa s	0.001	[35]
Characteristic length	d_k	m	2×10^{-4}	[35]
Electrical conductivity	σ	$\mathrm{Ohm^{-1}cm^{-1}}$	2.0×10^4	[37]
Gibbs –Thomson coefficient	Γ	m K	2×10^{-7}	[29]
Inductor parameters				
Wave vector	k^*	$\mathrm{m^{-1}}$	65	[31]
AC current frequency	f	Hz	50	[34]
Amplitude of electromagnetic force	A_{emf}	$\mathrm{N\,m^{-3}}$	180	

3. Numerical model

To perform simulation of the experiment described above we use a 3-phase model for solidification in equiaxed regime which couples macroscale transport phenomena and microscale processes related to the phase transition. Detailed presentation of the model which was developed accounting for laminar flow of phases can be found elsewhere [32], below only its brief description is provided. Yet, as it is evoked above, electromagnetic force generally intensifies flow affecting grain package and even may make the flow turbulent. Modification of the algorithm for the grains packing is presented in section 3.2, turbulent model and discussion of its applicability for simulation is discussed in section 3.3.

3.1. Coupling of microscale processes and macroscale transport

The model is based on utilization of the concept of envelope as an imaginary surface which encloses a solid dendrite skeleton (s-phase) with some amount of liquid between its arms, so-called interdendritic liquid (d-phase). The phase within the envelope, which unifies solid and interdendritic liquid, is considered as an equiaxed grain (e-phase) and the liquid outside of envelope is considered to be extradendritic liquid (l-phase). In a volume-averaging approach, each of these phases is represented with its volume fraction, i.e. with f_s for the solid and f_d, f_l for inter- and extradendritic liquid, respectively. Fraction for the grain phase is given as $f_e = f_s + f_d$ and summation rule $f_e + f_l = 1$ fulfills. Intrinsic averaged concentration c_i $(i = s, d, l, e)$ is associated with each of the phases, and concentration c_{env} is attributed to the surface of the envelope. The interface between the solid and interdendritic liquid phases is supposed to be at the equilibrium state, thus the interface solute concentrations are $c_l^* = (T_l - T_0)/m$ from the side of the liquid and $c_s^* = kc_l^*$ from the side of the solid, where k is the solute partition coefficient. Solute flux J_{le}^d due to molecular diffusion between the interdendritic and extradendritic liquid is taken into account with the use of the diffusion lengths l_l, whose definition was discussed in the [32]. Several phenomena are associated with solidification process, as proposed in

[38]. First, this is grain growth due to the elongation of the primary dendrite arms according to constitutional undercooling that implies increase of the envelope surface with velocity v_{env}, the latter takes into account deviation of the shape of the envelope from spherical one. Second, there is a solidification of the interdendritic liquid which can be seen as motion of the interface between the solid and interdendritic liquid with the velocity v_{ds}. Amounts of mass and solute transported between the extradendritic liquid and grain due to envelope enlargement are denoted hereafter as M_{le} and J_{le} and given below in Table 2. Similarly, M_{ds} and J_{ds} represent the amounts of mass and solute transported from interdendritic liquid to solid due to the motion of the interface between the two phases. The remelting rate is driven by a difference between c_l^* and c_l and is regulated with an adjustable coefficient g_α. A scheme presented in Fig. 2 illustrates phases distribution, associated solute concentrations, and a diffuse flux between interdendritic and extradendritic liquid J_{le}.

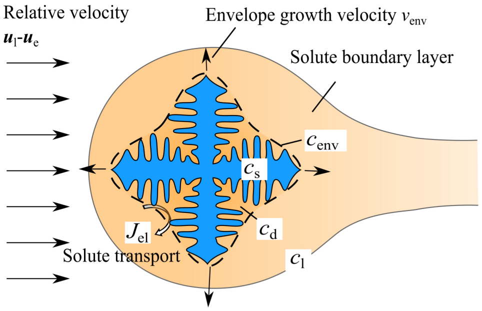

Figure 2: Illustration to concentration distribution around and inside a dendritic grain

It is supposed that grains appear in the bulk volume due to nucleation which happens instantaneously with a nucleation rate N_Φ once the local constitutional undercooling is higher than a predefined one ΔT_{nucl}. The value of ΔT_{nucl} chosen in the present paper (Table 2) implies heterogeneous nucleation. Nucleation makes the number density of grains n non zero, and a small fractions of the solid phase appears due to mass transition from liquid to solid M_Φ accompanied by the corresponding solute flux J_Φ. Further the grains can be dragged by the flow or their motion can be affected directly by gravity and electromagnetic force. It is supposed that the interdendritic liquid moves together with the solid skeleton, i.e. these phases share the same velocity field $\mathbf{u}_e$ which is different from the velocity $\mathbf{u}_l$ related to the extradendritic liquid. The laminar flow field is described with Navier-Stokes equations which take into account buoyancy and electromagnetic force acting on the liquid and grains using terms $\mathbf{F}_{bi}$ and $\mathbf{F}_{Ei}$, $(i = l, e)$, respectively. Buoyancy force dependent on variation of temperature and concentration for the liquid and grain phase is calculated with Boussinesq approximation (Table 2). Yet, for grain phase one more buoyancy term is introduced which takes into account difference between the density of the solid phase ρ_s^b and a reference density ρ_{ref}, as in [32, 35, 39]. Interaction between liquid and grain phases is accounted for via an exchange coefficient K_{le} whose nature is different for freely floating and for packed grains. For free floating region, i.e. $f_e < f_{e,p}$, the momentum exchange coefficient between the liquid and grain phases is estimated by the Happel's model[40], which fits well with Stokes' law when $f_e \to 0$. It is supposed that viscosity assigned to grain phase increases gradually with grain growth as it was evoked in [41, 42], yet, in present paper at small grain fraction $\mu_e = \mu_l$. When $f_e \geq f_{e,p}$, the grain phase is packed, i.e. it becomes immovable while the permeability of the grain fraction is changed and it can be evaluated by Carman-Kozeny equation based on a constant characteristic length number $d_k = 2 \times 10^{-4}$ related to grain number density and dendrite arm spacing [35]. The flow partitioning effect between the inter- and extradendritic liquid is neglected for simplicity. The algorithm of grains' packing is modified in the present paper compared to previously adopted one in [32] and is discussed in section 3.2 below.

Energy transport is solved for the grain and liquid phases separately with use of enthalpies h_e and h_l, respectively. Yet, a heat exchange coefficient between the l-phase and e-phase H^* is used and its value is taken large enough to eliminate the temperature difference between phases. The latent heat release during the phase transition is taken into account by a term $M_{le}h^*$, where h^* is chosen differently for solidification and remelting (Table 2).

System of governing equations (5)-(16) along with closure relations given in Table 2 represents processes described above. It is appropriate to remind that these equations are macroscopic and obtained from microscopic ones after averaging of the latter over a representative volume. Yet, notation traditionally used for intrinsic values averaged over a volume is omitted hereafter.

$$\rho_e = \frac{f_d\rho_l + f_s\rho_s}{f_d + f_s}; \quad c_p^e = \frac{f_d\rho_l c_p^l + f_s\rho_s c_p^s}{f_d\rho_l + f_s\rho_s}; \quad \kappa_e = \frac{f_d\kappa_l + f_s\kappa_s}{f_d + f_s} \tag{4}$$

$$\begin{aligned}&\frac{\partial\left(f_l\rho_l\mathbf{u}_l\right)}{\partial t} + \nabla\left(f_l\rho_l\mathbf{u}_l\mathbf{u}_l\right) = -f_l\nabla P + \nabla\left[\mu_l f_l\left(\nabla\mathbf{u}_l + \left(\nabla\mathbf{u}_l\right)^T\right)\right]\\ &+\mathbf{F}_{Bl} + \mathbf{F}_{El} + K_{le}\left(\mathbf{u}_e - \mathbf{u}_l\right)\end{aligned} \tag{5}$$

$$\begin{aligned}&\frac{\partial\left(f_e\rho_e\mathbf{u}_e\right)}{\partial t} + \nabla\left(f_e\rho_e\mathbf{u}_e\mathbf{u}_e\right) = -f_e\nabla P + \nabla\left[\mu_e f_e\left(\nabla\mathbf{u}_e + \left(\nabla\mathbf{u}_e\right)^T\right)\right]\\ &+\mathbf{F}_{Be} + \mathbf{F}_{Ee} + K_{le}\left(\mathbf{u}_l - \mathbf{u}_e\right)\end{aligned} \tag{6}$$

$$\mu_e = \mu_l/(3.5 f_e)\left[(1 - f_e/f_{e,p})^{-2.5 f_{e,p}} - (1 - f_e)\right] \tag{7}$$

$$\frac{\partial\left(f_l\rho_l h_l\right)}{\partial t} + \nabla\left(f_l\rho_l\mathbf{u}_l h_l\right) = \nabla\left(\kappa_l f_l\nabla T\right) + M_{ds}L f_l - M_{le}h^* + H^*(T_e - T_l) \tag{8}$$

$$\begin{aligned}&\frac{\partial\left(f_e\rho_e h_e\right)}{\partial t} + \nabla\left(f_e\rho_e\mathbf{u}_e h_e\right) = \nabla\left(\kappa_e f_e\nabla T\right) + M_{ds}L f_e + M_{le}h^* +\\ &+ H^*(T_l - T_e)\end{aligned} \tag{9}$$

$$h_l = \int_{T^h_{ref}}^{T_l} c_p^l dT + H_{ref}, \quad h_e = \int_{T^h_{ref}}^{T_e} c_p^e dT + H_{ref}$$

$$\frac{\partial n}{\partial t} + \nabla\cdot\left(n\mathbf{u}_e\right) = N_\phi \tag{10}$$

$$\frac{\partial\left(f_l\rho_l\right)}{\partial t} + \nabla\cdot\left(f_l\rho_l\mathbf{u}_l\right) = -M_{le} - M_\phi \tag{11}$$

$$\frac{\partial\left(f_e\rho_e\right)}{\partial t} + \nabla\cdot\left(f_e\rho_e\mathbf{u}_e\right) = M_{le} + M_\phi \tag{12}$$

$$\frac{\partial\left(f_s\rho_s\right)}{\partial t} + \nabla\cdot\left(f_s\rho_s\mathbf{u}_e\right) = M_{ds} + M_\phi \tag{13}$$

$$\frac{\partial\left(f_l\rho_l c_l\right)}{\partial t} + \nabla\cdot\left(f_l\rho_l\mathbf{u}_l c_l\right) = -J_{le}^d - J_{le}^v - J_\Phi \tag{14}$$

$$\frac{\partial(f_e\rho_e c_e)}{\partial t} + \nabla\cdot\left(f_e\rho_e\mathbf{u}_e c_e\right) = J_{le}^d + J_{le}^v + J_\Phi \tag{15}$$

$$\frac{\partial(f_s\rho_s c_s)}{\partial t} + \nabla\cdot\left(f_s\rho_s\mathbf{u}_e c_s\right) = J_{ds} + J_\Phi \tag{16}$$

Table 2: Sources terms for the equations (5) - (16)

Source and interaction terms in Navier-Stokes equation

$$\mathbf{F}_{El} = f_l F_x \mathbf{e}_x \qquad \mathbf{F}_{Ee} = f_e F_x \mathbf{e}_x$$

$$\mathbf{F}_{Bl} = f_l \rho_l \mathbf{g} \left[\beta_T \left(T^b_{ref} - T_l\right) + \beta_c \left(c_l^{ref} - c_l\right)\right]$$

$$\mathbf{F}_{Be} = f_d \rho_l \mathbf{g} \left[\beta_T \left(T^b_{ref} - T_l\right) + \beta_c \left(c_l^{ref} - c_d\right)\right] + f_s(\rho_s^b - \rho_{ref})\mathbf{g}$$

$$K_{le} = \begin{cases} 18 f_l^2 f_e \dfrac{\mu_l}{d_e^2} \dfrac{2 + 4/3 f_e^{5/3}}{2 - 3 f_e^{1/3} + 3 f_e^{5/3} - 2 f_e^2} & f_e < 0.637 \\ 150 \mu_l f_e^2 / (d_k^2 f_l^3) & f_e \geq 0.637 \end{cases}.$$

Source in energy equations

$$h^* = \begin{cases} h_l & Solidifying \\ h_e & Remelting \end{cases}$$

Nucleation rate

$$N_\phi = \begin{cases} f_l (n_{max} - n)/dt & \text{if } \Delta T > \Delta T_{nucl} \ and \ n < n_{max} \\ 0 & \text{else} \end{cases}$$

Mass exchange between the phases

$$M_\Phi = d(N_\phi \rho_l \pi d_0^3 / 6)/dt$$

$$M_{le} = \begin{cases} \rho_l S_e^M v_{env} & Solidifying \\ \rho_l S_e^M g_\alpha (c_l^* - c_l) & Remelting \end{cases} \qquad M_{ds} = \begin{cases} \rho_s 2 f_d v_{ds} / \lambda_2 & Solidifying \\ f_s M_{le} / f_e & Remelting \end{cases}$$

Solute exchange between the phases

$$J_{le}^d = -\rho_l S_e^J D_l (\overline{c}_{env} - c_l)/l_l; \quad J_{le}^v = M_{le} \overline{c}_{env}; \quad J_\Phi = M_\phi c_s^*; \quad J_{ds} = c_s^* M_{ds}$$

Auxilary expressions

$$f_e c_e = f_d c_d + f_s c_s \qquad \overline{c}_{env} = (l_d c_l + l_l c_d)/(l_d + l_l)$$

$$S_e^M = (36 \pi n)^{1/3} f_e^{2/3} \qquad S_e^J = (36 \pi n)^{1/3} f_e^{2/3} / \phi_J$$

$$v_{env} = \phi_M \frac{D_l m_l (\kappa - 1) c_l^*}{\pi^2 \Gamma} \left[\frac{c_l^* - c_l}{c_l^* (1 - k)}\right]^2 \qquad v_{ds} = \frac{D_l (c_l^* - c_d)}{l_d (c_l^* - c_s^*)}$$

$$l_l = \min\left\{\frac{D_l}{v_{env}}, \frac{d_e}{2 + 2 Sc^{1/3} Re^a / (3 f_l)}\right\} \qquad a = \frac{2 Re^{0.28} + 4.65}{3(Re^{0.28} + 4.65)}$$

$$Sc = \mu_l / (\rho_l D_l); \quad Re = |\mathbf{u}_l - \mathbf{u}_e| (\rho_l f_l d_e)/\mu_l; \quad l_d = f_d \lambda_2 / (2 f_e)$$

Constant values parameters

$$d_k = 2 \cdot 10^{-4}; \quad d_0 = 10^{-6}; \quad \Delta T_{nucl} = 0; \quad n_{max} = 10^9; \quad H^* = 10^8$$

$\phi_M = 0.271$[43]; $\phi_J = 0.71$ [43]; $g_\alpha = 1 \cdot 10^{-3}$; $f_{e,p} = 0.637$; $\lambda_2 = 1.5 \cdot 10^{-4}$

3.2. Grains' packing

In most models dealing with solidification in equiaxed regime, equiaxed grains get packed immediately when grain phase fraction f_e becomes equal or higher than a critical one, $f_{e,p}$. This represents mechanical interaction between grains and implies that solidification is initiated at the boundary and continues more or less uniformly. In order to adapt this idea to the case of a rather strong convective flow due to electromagnetic stirring, a new grain packing method has been developed and applied in simulations. It is supposed that to be packed grains should have an immovable neighbor upon which they can attach. In Fig. 3 only grains in the region marked with a green color can change their state from freely moving to packed because they are positioned either near the wall or near at least one cell within which the grains were already packed. In the absence of in-situ experimental observations of equiaxed solidification under the action of EMS, the critical value for the grain fraction is kept to be equal to 0.637 as in other publications [44, 39].

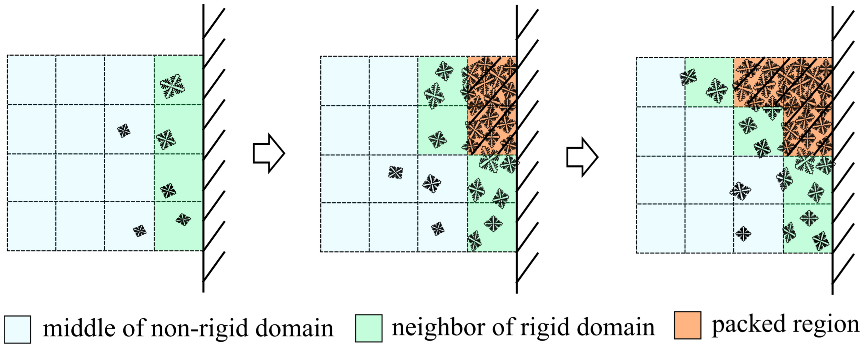

Figure 3: Illustration to the grain packing algorithm. In the left: grains near the wall are not packed because their grain fraction is below a critical one; in the center: the grains near the wall for which $f_e \geq f_{e,p}$ are packed; in the right: those grains in the volume for which $f_e \geq f_{e,p}$ and which are neighboring to the packed ones are also packed

3.3. Accounting for flow instabilities with realizable $k_\varepsilon - \varepsilon$ model

Preliminary simulations performed for the cavity filled with a melted alloy have shown weak rapid oscillations of velocity and temperature fields, convergence of solution could not be attained with laminar flow model. Therefore, to attain convergence of hydrodynamic equations at the early stage of solidification a realizable $k_\varepsilon - \varepsilon$ turbulent model was applied in simulations [45]. The $k_\varepsilon - \varepsilon$ model is built on a general assumption that velocity, pressure, temperature, etc. in the turbulent flow can be presented as a sum of its time mean value and fluctuating component: $\xi =< \xi >_t +\xi'$. Then, Boussinesque approximation relates Reynolds stress tensor composed of product of fluctuating velocity components averaged in time $< u'_i u'_j >_t$ with gradient of mean velocity and turbulent kinetic energy k_ε via eddy viscosity (turbulent viscosity) μ_t, which is supposed to be isotropic. This leads to appearance of turbulent viscosity in momentum equations and so-called $k_\varepsilon - \varepsilon$ model proposes equations for the turbulent energy k_ε and its dissipation ε along with some empirical relations aimed to close the system of equations. Intensification of conductive heat transport due to the interaction of turbulent vortices is introduced in the equation of energy transport via turbulent thermal conductivity and diffuse transport of species should also be intensified due to turbulent diffusivity. A specific difficulty related to multiphase flow is that turbulence can be treated for a mixture of phases, either be assigned to one of phases or could be treated separately for each phase. In the present paper the first option is selected and equations which replace Navier-Stokes equations (5)-(9) in the set of governing equations as well as equations for k_ε and ε are given below.

$$\frac{\partial\left(f_i\rho_i\mathbf{u}_i\right)}{\partial t}+\nabla\cdot\left(f_i\rho_i\mathbf{u}_i\mathbf{u}_i\right)=-f_i\nabla P+\nabla\left[(\mu_i+\mu_{t,i})f_i\left(\nabla\mathbf{u}_i+\left(\nabla\mathbf{u}_i\right)^T\right)\right]+$$

$$+\mathbf{F}_{Bi}+\mathbf{F}_{Ei}+K_{ij}\left(\mathbf{u}_j-\mathbf{u}_i\right) \tag{17}$$

$$\frac{\partial\left(f_i\rho_ih_i\right)}{\partial t}+\nabla\left(f_i\rho_i\mathbf{u}_ih_i\right)=\nabla\left(\left(\kappa_i+\kappa_{t,i}\right)f_i\nabla T_i\right)-M_{ij}h^*+H^*(T_j-T_i) \tag{18}$$

$$\frac{\partial\left(\rho_mk_\varepsilon\right)}{\partial t}+\nabla\cdot\left(\rho_m\mathbf{u}_mk_\varepsilon\right)=\nabla\cdot\left[\left(\mu_m+\frac{\mu_{t,m}}{\sigma_k}\right)\nabla k_\varepsilon\right]+G_{k,m}-\rho_m\varepsilon \tag{19}$$

$$\frac{\partial\left(\rho_m\varepsilon\right)}{\partial t}+\nabla\cdot\left(\rho_m\mathbf{u}_m\varepsilon\right)=\nabla\cdot\left[\left(\mu_m+\frac{\mu_{t,m}}{\sigma_\varepsilon}\right)\nabla\varepsilon\right]+\rho_mC_1S\varepsilon-$$

$$-\rho_mC_2\frac{\varepsilon^2}{k_\varepsilon+\sqrt{\mu_{t,m}\varepsilon/\rho_m}} \tag{20}$$

$$\mu_{t,m}=\rho_mC_\mu k_\varepsilon^2/\varepsilon \tag{21}$$

$$\rho_m=f_l\rho_l+f_e\rho_e,\quad \mu_m=f_l\mu_l+f_e\mu_e,\quad \mathbf{u}_m=(f_l\rho_l\mathbf{u}_l+f_e\rho_e\mathbf{u}_e)/\rho_m \tag{22}$$

$$\mu_{t,i}=\mu_{t,m}\rho_i/\rho_m,\quad \kappa_{t,i}=c_{p,i}\mu_{t,i}/Pr_t \tag{23}$$

In the equation (17)-(23) index $i=l,e$ denotes a phase to which transport equation is related and index m is used for mixture of $l-$ and $e-$ phases, whose properties are defined by relations (22). Closure relations and value for constants used in equations (17)-(23) are given in Appendix A.

Before going into details related to solidification, let us estimate effect of turbulence throughout the process. Simulation starts with a cavity filled with liquid melt, at this stage only equations related to the extradendritic liquid are used, no phase transition or interaction between phase is involved. In Fig.4 temperature distribution with a superposed velocity field and distribution of turbulent characteristics k_ε and $\mu_{t,m}$ are presented for median section of the cavity, for the value of the adjustable constant in the expression (3) $A_{emf}=180$. Ratio of oscillation component of velocity $u'\approx\sqrt{2/3k_\varepsilon}\approx 6\times10^{-3}m/s$ to the mean flow velocity $4.5\times10^{-2}m/s$ indicates medium intensity of the turbulence about 13%. This could be expected since value of the Reynolds number $Re\approx$ 6000 based on a hydraulic diameter for a lateral side wall $D\approx 1.7\cdot10^{-2}$m also indicates moderate turbulance. Turbulent viscosity having maximal value $5.5\cdot10^{-2}$ Pa·s is localized near the hot wall while in the most of the cavity it is less than $1.0 \cdot 10^{-2}$ Pa·s. Provided that densities for all phases are equal this gives ratio of turbulent and molecular viscosity from $\mu_{t,i}/\mu_i \approx 55$ to 10, which is rather low compared to other works where solidification under EMS was studied. Indeed, in [46] this ratio was equal to 208 at the beginning of solidification and decreased to 20 when more than a half of the cavity was solidified. In continuous ingot solidification [47] maximal value of turbulent viscosity was nearly 200 times higher than molecular one. In the turbulent model by Poole and El-Kaddah [48], the ratio μ_t/μ in pure liquid was about 60, then decreased during solidification to 30 within the mushy zone keeping its initial value in the liquid and when its value did not exceed 15 the flow was declared laminar.

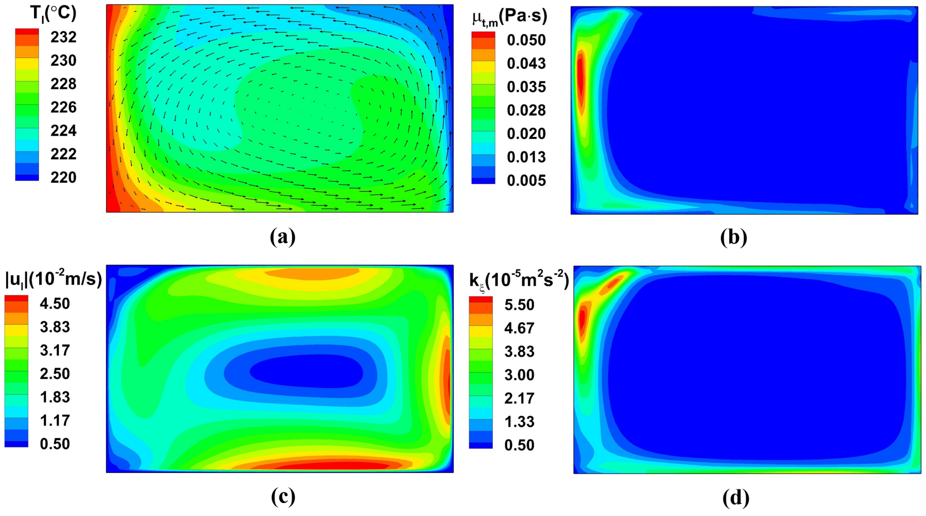

Figure 4: Temperature distribution and liquid flow vectors (a), turbulent viscosity distribution (b), magnitude of velocity (c), and turbulent kinetic energy distribution (d) prior solidification for $A_{emf} = 180$

Regarding intensification of heat exchange, the estimated maximal value for turbulent thermal conductivity according to (23) is $\kappa_{t,i} \approx 12$ W/m·K, i.e. of order of 20% of thermal conductivity of material. Similar estimation for diffusion coefficient of solute gives $D_{l,t} = \mu_{t,l}/(\rho_l Pr_t) \approx 7 \cdot 10^{-6}$ m^2/s that indicates significant increase of diffuse transport. However, in stirred pure liquid as well as between moving grains convective solute transport should still prevail over diffusive one. Yet, question arises about those zones where grain phase velocity is nearly zero or grains are already packed. Generally it is supposed that turbulence should be damped within the semi-solid region (mushy zone) as well as within grain-packed region. In models dealing with solidification [46, 47, 48] this was realized via various modifications of the coefficient C_μ in calculation of turbulent viscosity (21) and with use of different destruction terms in the equation of turbulent energy k_ε [46], or for turbulent energy dissipation [47, 48]. Moreover, an additional damping term for the floating mushy zone was introduced in [48] to overcome constraints related to the use of a unique velocity field for the two phases.

In realizable $k_\varepsilon - \varepsilon$ model proposed in ANSYS FLUENT$^{®}$ coefficient C_μ used for calculation of the turbulent viscosity (21) is not constant either (contrary to standard $k_\varepsilon - \varepsilon$ or RNG models), yet all coefficients were tuned to treat properly free jet spreading. Modeling of destruction and production terms in equation for ε was also optimized for solutions of problems related to jets. It could be supposed that in realizable $k_\varepsilon - \varepsilon$ model damping of the turbulence in the floating mushy zone as well as in packed bed region is not so efficient as in low-Reynolds models in [46, 47, 48]. Yet, as it was demonstrated above, for the problem under study turbulent viscosity was not so high even at the beginning of solidification and appearance of packed grains should diminish intensity of the flow. Therefore, effects related to enhancement of heat and solute diffuse transport will disappear in the packing bed region and decrease in the floating mushy zone. That is why in further calculations we used system of equations which describes turbulent flow with $k_\varepsilon - \varepsilon$ approximation, i.e. equations (5)-(9) are replaced with (17) -(22) (and closure relations from Appendix A). However, equations for phase and solute transport (10)-(16) including equations for diffusion fluxes and relations for diffusion length in Table 2 remained unchanged.

3.4. Solution algorithm

In our approach the processes which occur at macroscopic and microscopic scale are modelled with different time steps as shown in Fig. 5. A larger time step is used for the calculation of the transport phenomena at the macro-sale and a smaller time sub-steps is used for the calculation of the processes within the grain (diffusion, solidification) and the grain growth. The macroscopic calculation, including multiphase flow field and transport of energy, solute and grain number density, are solved by ANSYS FLUENT® software in which the modeling of the solidification at the microscale is implemented with user-defined functions.

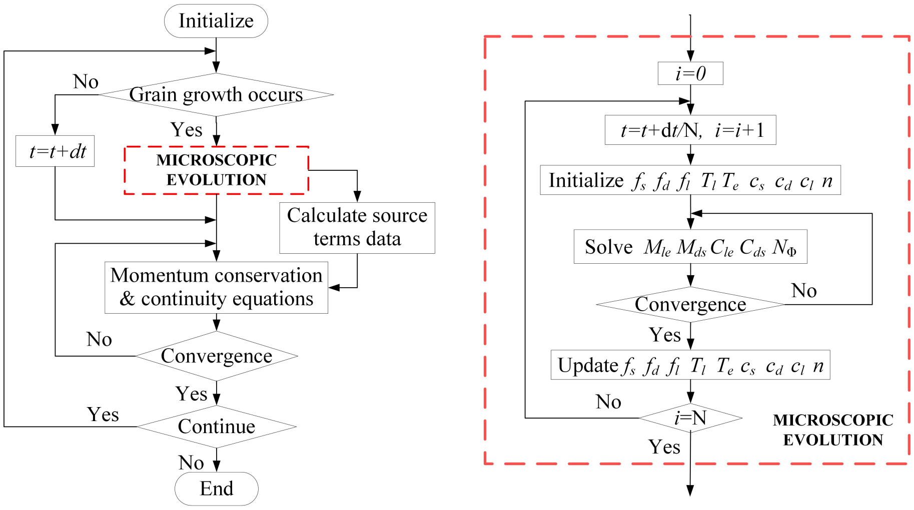

Figure 5: Solution algorithm

4. Results and discussion

Three-dimensional simulations are performed with the grid comprising 100× 60×15 mesh cells and results presented in section 4.1 and 4.2 are obtained with $A_{emf} = 180\text{N/m}^3$ in the expression for the electromagnetic force (3). Final macrosegregation patterns calculated with two other values of the adjustable coefficient $A_{emf} = 150\text{N/m}^3$ and $A_{emf} = 110\text{N/m}^3$ are shown in section 4.3

to demonstrate effect of the intensity of the electromagnetic force. Physical properties of the alloy were given above in the Table 1 and values of numerical constant used in the model can be found in Table 2 and Table A.4 (in Appendix A). Initial state in simulations corresponds to the uniform distribution of the nominal concentration 10wt% of Pb in the pure liquid and uniform temperature gradient inside the cavity corresponding to the temperature of 237.9°C and 225.0°C applied at the right and the left lateral sides, respectively. This corresponds approximately to 16300s of the physical time in the solidification experiment presented in [30]. In calculations at this state electromagnetic force is activated, whereas cooling is taken into account via boundary conditions (recalculated from experimental data) applied at the lateral sides of the cavity. It takes about 50 second to get the forced convection developed and temperature distribution shown in Fig. 4(a) in section 3.3 was obtained after 150s of calculations.

In the process under consideration multiple physical phenomena are strongly coupled. Indeed, distributions of temperature and solute which define phase transition are affected by fluid flow which is governed by electromagnetic and buoyancy forces while the latter depends on the flotation of equiaxed grains and local concentration of the rejected solute. Furthermore, growth or melting of grains is accompanied by heat release or absorption that also affects temperature field. Since evolution of temperature distribution over a cavity was measured during the experiment, it should serve as primary reference for comparison between results obtained numerically and experimentally. Therefore, analysis of results is started with presentation of evolution of temperature field during solidification. It is followed by description of the solidification process with evolution of multiphase flow, distribution of concentration and phases' fraction. Concentration of lead in mixture used in presentation of results is calculated as

$$c_{mix} = \frac{\rho_l f_l c_l + \rho_e f_e c_e}{\rho_l f_l + \rho_e f_e} \tag{24}$$

Finally segregation pattern for the solidified domain obtained in calculations is presented and compared with X-Ray image of the sample. Calculated distribution of grains' number density is compared with optical image of the sample.

4.1. Evolution of temperature distribution during solidification

Due to temperature difference between lateral walls, buoyancy force appears in the cavity. In the absence of other forces apart of gravity, the melt at the hotter lateral side would flow upward and near the colder wall it would go downward thus creating a vortex and forming a positive temperature gradient in vertical direction. The presence of electromagnetic force which acts near the cavity bottom toward the colder lateral side also leads to formation of a unique vortex which makes liquid goes upward near a colder surface and downward near the warmer. Prior solidification temperature distribution in the cavity defined by this flow is almost uniform in the center with strong gradients near lateral sides (Fig. 4(a)). As cooling and solidification proceeds, the character of temperature distribution changes being influenced by various factors. To illustrate this, four representative temperature distributions at the calculation time t=300s, 540s, 900s, and 1440s are shown in Fig. 6 in which temperature fields reconstructed from measurements at the corresponding time moments are overlaid with calculated ones. Calculated temperature field is taken from the front face of cavity, however, there is no temperature variation along z-axis, i.e. it is quasi-2D. At t=300s (Fig. 6(a)), the character of the flow and temperature distribution did not change compared to those presented in Fig. 4(a) since solidification did not really progressed. It should be noted that, according to the temperature map reconstructed from measurements, actual character of the flow seems to be slightly different from that observed in calculations. Indeed, it could be supposed that the right and the central part of the cavity is occupied by the vortex of the forced flow, yet, buoyancy flow probably survives near the hotter (left) wall. The two vortices which converge at the top and diverge at the bottom push isotherms toward the center in the upper part of the cavity and toward the walls in its lower part (Fig. 6(a), colormap). At the bottom of the cavity and in its center temperature is almost uniform according to measurements and varies slightly in simulations. The difference between the measured and calculated temperature fields could be explained, first of all, by uncertainties in boundary conditions. In fact, in estimation given by Eq. (1) convective heat transport along the lateral walls was omitted while it can be seen that at the distance of 5mm from the wall the flow affects temperature distribution. The second reason is related to estimation of the coefficient A_{emf} in the electromagnetic force given for Eq. (3).

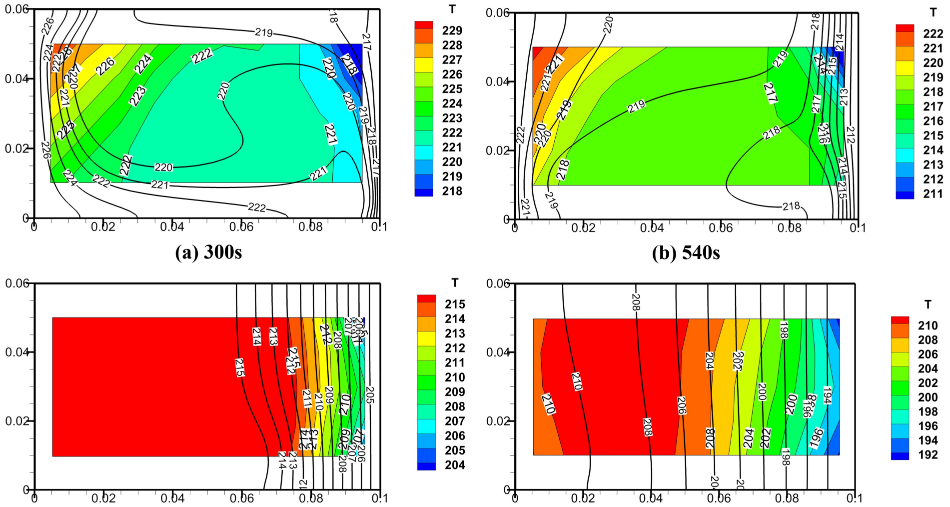

(a) 300s

(b) 540s

(c) 900s

(d) 1440s

Figure 6: Comparison of temperature field at different solidification times: (a) 300 s, (b) 540 s, (c) 900 s and (d) 1440 s, temperature isolines obtained in calculations superposed on temperature colourmap constructed from thermocouple measurements

At t=540s (Fig. 6(b)), the shape of the isotherms is clearly defined by two vortices existing in the liquid. The center and lower part of cavity have almost uniform temperature whose value is close to the liquidus temperature of the alloy at its nominal concentration, $T_L = 219°\text{C}$. In fact, as it can be seen in Fig. 8, equiaxed grains exist in this region. Temperature value is maintained near the liquidus temperature due to the release of latent heat during grain growth in the region closer to the colder wall and also due to the heat absorption during grains' remelting in the region closer to the hotter wall. Because of this the temperature gradient at the right lateral wall is larger than at the left one. At t= 900s (Fig. 6(c)), the isotherms gradually become vertical and less distorted. Due to the packing of equiaxed grains, the liquid flow becomes weaker thus the heat is transferred mainly by conduction. Although, temperature difference between the left and the right lateral walls exists, temperature is mostly uniform in the cavity, because its variation is concentrated near the colder (right) side. Finally, at t=1440s presented in Fig. 6(d), temperature gradient at the colder wall decreases that means that the latent heat release is stopped, i.e. liquid fraction become small in this zone. Yet, the area with the highest temperature is located at some distance from the left lateral wall indicating that temperature decrease in the volume is slower than at the boundary.

Relative instantaneous local error between calculated and experimentally measured temperature which can be introduced as $max\{|T_{calc}-T_{meas}|/(T_{LEFT}-T_{RIGHT})\}$, displays maximal value $\approx 13\%$ in the center of the cavity at early stage of solidification. Probably, apart from uncertainties related to thermal boundary conditions and to the estimation of the electromagnetic force, this can be attributed to the columnar grains whose growth was not taken into account in simulations but which could be observed in a small region near the colder wall. Indeed, since columnar grains are supposed to be attached to the boundary, they would resist fluid flow and would make it less intense. Hence, intensity of EMS driving flow could be overestimated in the present solidification model which considers only equiaxed grains.

In Fig. 7, cooling curves reconstructed from measurements and obtained in simulations are presented for several points in the cavity, corresponding to the position of the thermocouples L21, L22, L25, L29 and L30 (shown in Fig. 1(a)).

Overall, the cooling curves obtained in simulation show similar tendency as measured ones and difference between numerical and experimental results lies within 6 degrees (7 for the point L22 at the beginning of the process). The dif-

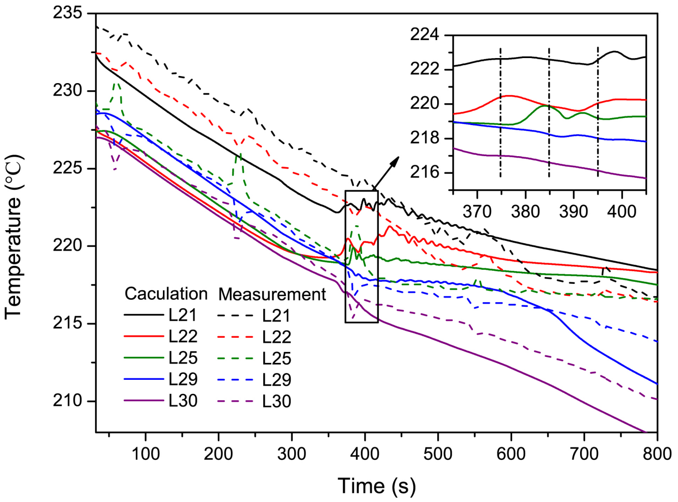

Figure 7: Comparison of (thick dashed lines) calculated and (thick plain lines) measured cooling curves at positions L21, L22, L25, L29 and L30.

ference, as it was already evoked above, seems to be related to underestimation of natural convection and probably to overestimation of the forced flow which makes temperature distribution across the cavity non-monotone: temperature at the point L22 happens to be lower than at the point L30 (closer to the cold wall) and at the point L25 (at the cavity center), which can be seen in Fig. 4. At the beginning of the cooling the temperature decreases mostly uniformly with a prescribed cooling rate of 0.03K/s. At about 400s cooling rate slows down for all points and all curves start to display strong fluctuation till 600s. Analysis of distribution of temperature, grain fraction and flow field at t=375s, 385s and 395s in Fig. 9 explains the nature of oscillations which is related to instantaneous damping of the forced convection and intensification of natural one because of enrichment of rejected Pb in the liquid. Further, temperature decreases slower for points which are close to hot side (L21, L22) than for those at the colder side (L29, L30). The cooling curve of the point in the center (L25) gets closer to the cooling curve at the hot side.

Curiously, experimental curves display rather strong temperature fluctuation every 200 second. We suppose that this can be related to flow instability and oscillatory behavior of a vortex of a natural convection which appears or intensifies periodically in the upper left corner of the cavity. This behavior could be probably reproduced with boundary conditions closer to actual ones.

4.2. Phase transition, transport of grains and of concentration

Solidification starts, according to temperature distribution, with nucleation of equiaxed grains at the top of the colder wall. Even if little later nucleation occurs over the whole surface of this lateral wall, equiaxed grains are brought mainly upwards to this corner due to convection driven by the electromagnetic force as well as due to their flotation. At early stage of solidification, most of these grains are captured and further dragged by forced convection toward the center of the cavity, where they are remelted in the high temperature region. Therefore, till t=300 s, equiaxed grains exist only at the upper right corner of cavity as seen in Fig. 8(a.1), where a very weak negative segregation appears (Fig. 8(b.1)).

When the value of volume faction for equiaxed grains attains packing limit $f_{e,p} = 0.637$, the grains next to the wall are getting packed and become immovable. Other grains are brought upwards surviving at some distance from the cold wall, and grow up with temperature decrease in the volume. During the period from $t = 350$s to 540s the layer of packed grains extends downwards from the grain floating at the top, then leftwards. In Fig. 8(a.2), the interface between unpacked region and packed region is presented with a iso-surface $f_e = 0.637$. Liquid flow in packed region becomes weak due to rapid increase of flow resistance in the mushy zone. At 540s grain fraction at the cold wall is nearly 0.9 while solid fraction (shown with black lines) is about 0.4 at the wall and less than 0.3 at the edge of the region of packed grains.

During solidification the heavy solute Pb rejected into the liquid phase makes the buoyancy effect more pronounced that alters forced convection. At t=540s (Fig. 8(a.2 and b.2)), the vortex generated by electromagnetic force in the liquid is located only in a lower part of the cavity and has maximal velocity of about 32 mm/s. In fact, at this stage flow can be considered almost laminar. Yet,

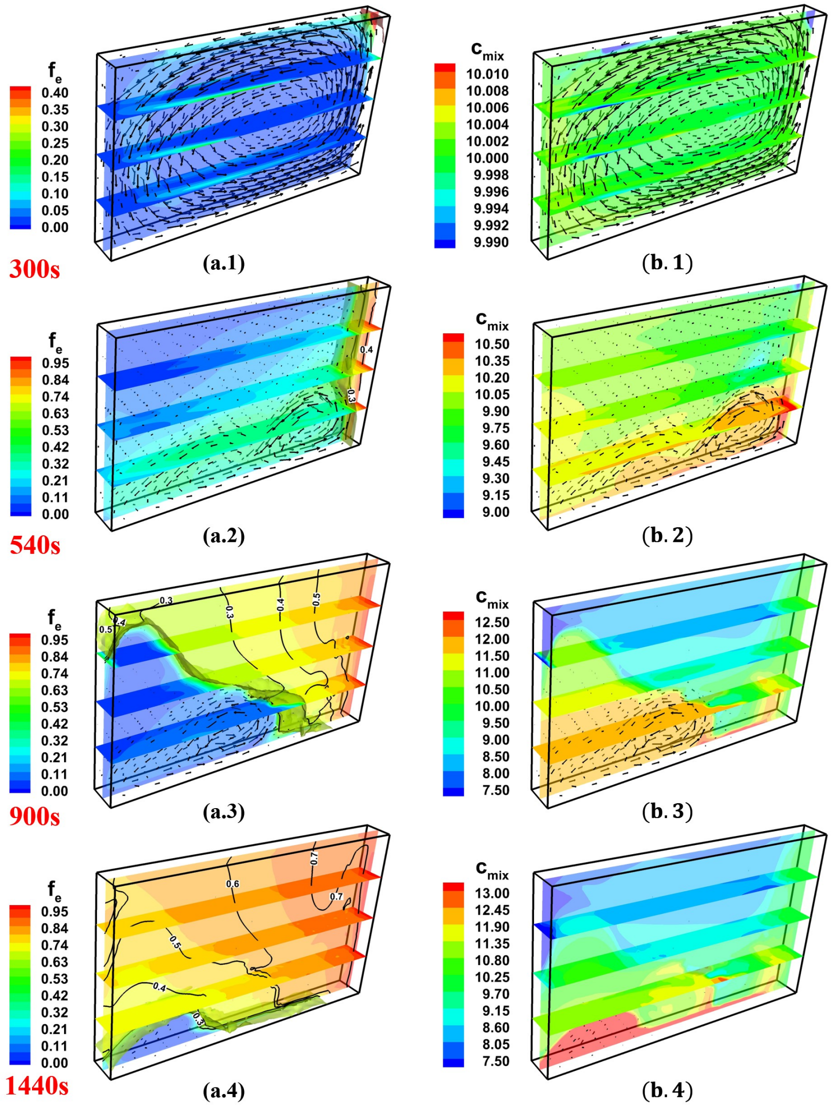

Figure 8: Evolution of grain fraction and grain velocity (a.1, a.2, a.3 and a.4) with black lines indicating solid fractions (a.2-a.4) and iso-surface $f_e = 0.637$ showing the edge of the region of packed grains; Distribution of concentration of Pb in mixture and velocity in the liquid (b.1, b.2, b.3 and b.4); Maximal velocities are: (a.1) 50.39 mm/s, (a.2) 32.44 mm/s, (a.3) 29.09 mm/s, (a.4) 7.63 mm/s, (b.1) 50.37 mm/s, (b.2) 32.51 mm/s, (b.3) 29.09 mm/s and (b.4) 6.68 mm/s.

intensity of the forced flow is sufficient to take the equiaxed grains away from the lower part of the colder wall, retarding their packing in this region. A layer enriched with Pb starts to form at the bottom of the cavity due to sedimentation of heavier liquid through the mushy zone (Fig. 8(b.2)). The concentration of Pb has a maximal instantaneous value at the highest point of the vortex of forced convection. Concentration in the center of the cavity is affected by the presence of grains which contain smaller amount of Pb and the zone slightly impoverished in Pb starts to form.

At t=900s, a half of the cavity is filled with the packed grains which makes a "rigid network", yet with rather low solid fraction which varies from 0.6 at the cold wall to 0.3 at the edge of the zone of packed grains (Fig. 8(a.3)). Flow of the liquid between packed grains is weak but it contributes to final macrosegregation. Liquid enriched with Pb continuously flows downwards, depleting the upper part of the volume while enriching the lower-left part. Vortex driven by electromagnetic force still exists below the packed region, yet it is displaced to the warmer lateral wall and tends to shrink to the bottom. Another vortex above is formed above the latter and occupies only small region near the hotter wall (Fig. 8(b.3)).

At t=1440s (Fig. 8(a.4) and (b.4)), liquid flow still exists near bottom of the cavity with maximal velocity of 7 mm/s. This part of liquid is highly enriched and requires lower temperature for solidification. Yet, since the flow is constrained by surrounding solid, the character of the solute distribution formed by this moment can hardly be affected.

Let us have a closer look at the moment when oscillations of the cooling curves were observed. The Fig. 9 shows distribution of temperature, of the solid fraction overlaid with grain velocity, and of the intrinsic concentration in the extradendritic liquid c_l overlaid with velocity of the liquid $\mathbf{u}_l$ for three moments of time with interval of 10 second. At this stage of of solidification, the vortex caused by thermosolutal convection occupies the upper-left part of the volume. The vortex enlarges and speed of flow in this vortex increases due to rejection of the heavier solute (Pb) when grain nucleates and solidifies. This instantly damps the forced convection at the top and hotter fluid moves along the cavity top toward the colder wall and this affects also temperature distribution in the cavity center. Yet, growing grains are moving downwards and to the left due to interaction of the natural and forced convection in the liquid. That makes the source of the rejected Pb to move as well, consequently, the vortex of natural flow change its position and starts to occupy mainly the upper part of the volume while the vortex of forced convection becomes stretched till the hotter wall in the bottom that brings the colder fluid to the cavity center and also alters again the motion of the growing grains and the source of the rejected Pb. This process of vortices' rearrangement repeats and causes oscillation of the cooling curves. The amplitude of oscillation becomes weaker with the time, indicating the multiphase flow field tends to be stable.

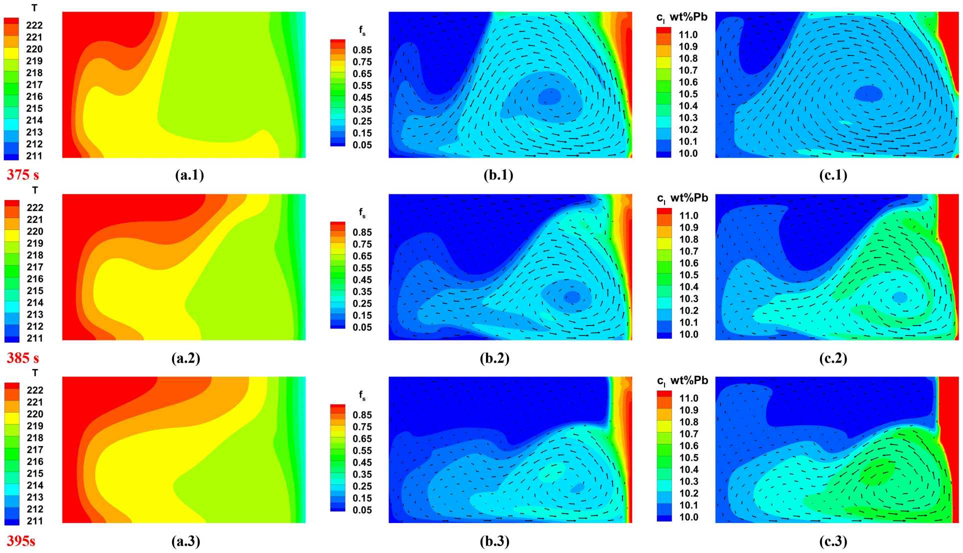

Figure 9: Distribution of temperature (a.1, a.2, a.3), of the solid fraction f_s with superposed field of grains' velocity $\mathbf{u}_e$ (b.1, b.2, b.3) and intrinsic concentration in extradendrtitic liquid c_l overlaid with the velocity field in the liquid $\mathbf{u}_l$ (c.1, c.2, c.3) for three moments of time indicated in the insert of the Fig. 7; Maximal velocity is 35 mm/s in all figures.

4.3. Density of grain number and macrosegregation map in solidified sample

In solidified sample calculated distribution of grain number density displays almost monotone increase from the right (colder) to the left (warmer) wall along with a layer of high grain number density at the top (Fig. 10(a)). This corresponds to experimental result with quite fine equiaxed grains at the top of cavity, coarse grain structure near the cold side and finer one near the warmer (Fig. 10(b)). Such distribution can be explained by EMS driving flow which takes away grains from cold side toward the center while these grains tend to float up because they have smaller density than liquid phase. Also, at the bottom of cavity where the last stage of solidification occurs, simulation shows quite large grain number density. In experiment, the region is occupied by porosities because of shrinkage. Final macrosegregation map (Fig. 10c) displays variation of Pb concentration in the range from 7.5wt% to 15wt% with zone of positive segregation at the bottom of the cavity closer to the left (colder)

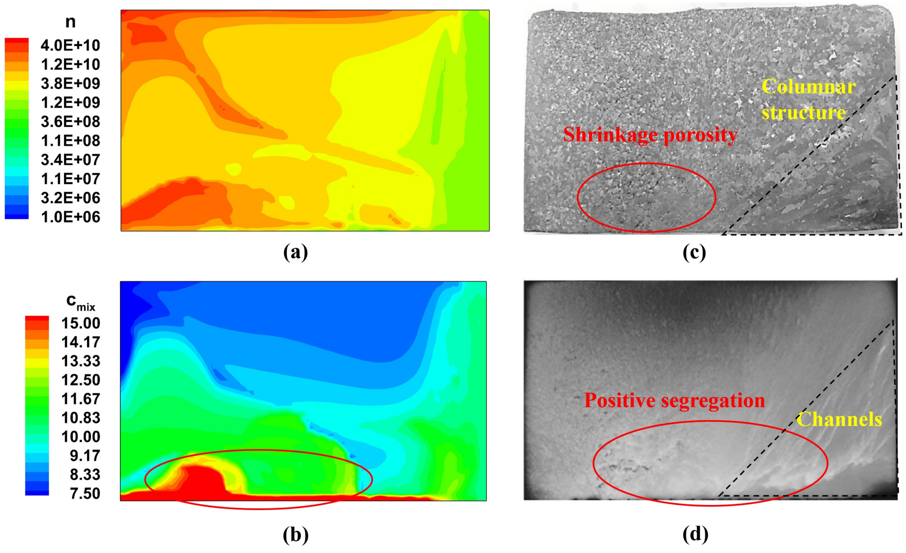

Figure 10: Comparison of macrosegregation map: calculated grain number density distribution(a), calculated macrosegregation map at center plane(b), Grain structure of ingot(c) and X-radiography of the ingot (d). Figures (c) and (d) are reprinted from publication [30] with permission from Elsevier

wall and region of negative segregation located at the top. Segregation at the bottom is formed due to descends of enriched liquid during the whole solidification process, interestingly this convective transport of solute becomes extremely significant through the growing packed grains. Segregation map obtained numerically is qualitatively similar to X-radiography of as-solidified sample shown in Fig. 10d. Thin segregation channels at right lower corner are not reproduced in calculations that is probably related to the growth of columnar grains, which is not included in current research. Yet, in simulations two thick short vertical channels are obtained closer to the right (hotter) wall. Location of the zone of maximal segregation obtained in simulations coincides with porous region in the experimental sample. Quantitative comparison can be performed between calculated segregation map and results of ICP analysis of as-solidified sample presented in Fig. 11c of ref.[30].

Although use of electromagnetic force does not lead to uniform distribution of concentration in the solidified sample, its positive effect on segregation pattern can be seen due to calculation results shown in Fig. 11 which were obtained with coefficients $A_{emf} = 110$ and $A_{emf} = 150$ in eq.(3). These figures along with Fig. 10c demonstrate that clearly EMS is important at the beginning of solidification but with appearance of zone of packed grains its effect decreases while buoyancy force intensifies due to rejection of the heavier solute. Weaker electromagnetic force cannot affect the upper part of the sample and become rapidly constraint in the lower left corner of the cavity where a very high concentration of Pb is observed for $A_{emf} = 110$.

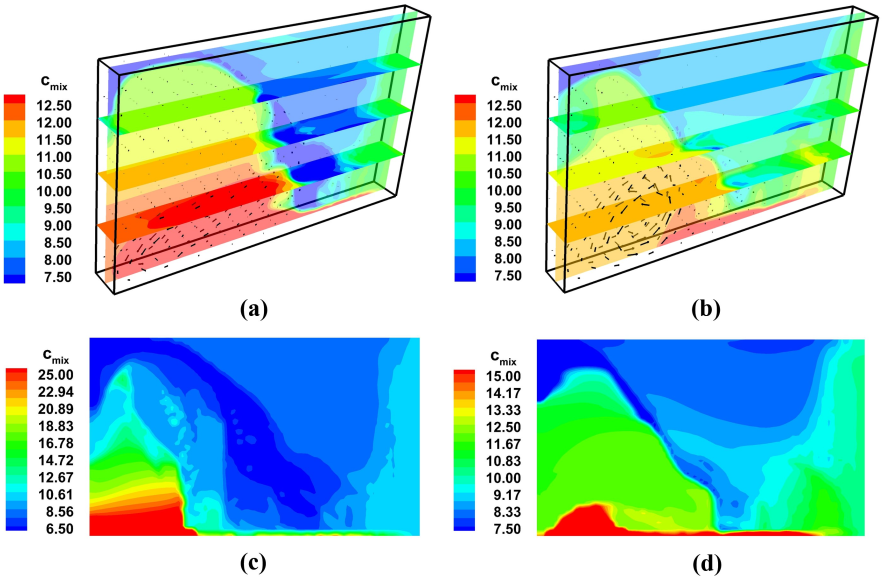

Figure 11: Effect of amplitude of electromagnetic force on distribution of the concentration of Pb in the mixture and velocity in the liquid phase (a and b) and final macrosegregation map of Pb(c and d)

5. Conclusion

In present work a 3-phase volume averaging equiaxed solidification model which accounts for the grains transport is applied for modeling of the AFRODITE experiment on crystallization of Sn–10 wt.%Pb alloy under the forced convective flow driven by EMS. Main observations and results can be summarized as follows. Electromagnetic force created in the liquid during the process drives fluid flow in the direction opposite to the action of thermo-solutal buoyancy force. The flow is slightly turbulent before solidification starts. With rejection of heavier solute due to solidification, the forced flow is damped and natural convection starts to occupy larger volume in the cavity. Interaction between the two vortices causes temperature oscillations and defines the shape of a zone with negative segregation at the top of the cavity. When equiaxed grains get packed, downward flow of highy enriched liquid through the rigid structure leads to accumulation of Pb at the bottom. The shape of the zone with a positive segregation is defined by the action of the electromagnetic force. Macrosegregation map obtained in simulation is similar to the pattern observed with X-Ray radiography of the solidified sample except a small zone where columnar growth happened.

Although the model provided results close to experimental one, multiple questions arises concerning numerical parameters and closure relations. One of them, related to the closure relation for growth parameters of dendrite grains as well as drag coefficients in case of turbulent flow was already mentioned above. To these questions joins also turbulence damping inside the mushy zone. Another question concerns macroscale electromagnetic force. Generally, electrical conductivity of solid can be several times higher than of liquid. During solidification this factor is not important in the beginning of the process because the solid fraction is small, therefore, variation of induced magnetic field and electric current inside the solidifying volume due to presence of the solid grains is negligible, the same is true for the results of the Lorentz force. Yet, induced fields should be altered if grains with rather high solid fraction accumulates in macro-groups. It could be supposed that in this case the local variation of the electromagnetic force acting on grains is not important because at high fractions the grains are packed while their solid fraction can be still small. Yet, local variation in conductivity can affect force distribution everywhere in the volume, i.e. including the pure melt. Furthermore, it is generally supposed that electromagnetic stirring promotes fragmentation of dendrites and these fragments serve as nucleation sites or already present equiaxed grains. This can be introduced into the model using various assumption [28, 49]. In the present work this phenomena was not taken into account to decrease number of uncertain parameters, yet, it deserves further study.

Acknowledgments

This work is a joint cooperation between the SIMAP laboratory of Grenoble INP (France) and the Key Laboratory of EPM of Northeastern University (P. R. China). The authors gratefully acknowledge financial support from the National Nature Science Foundation of China (Grant No. U1760206), the National Key R&D Program of China (Grant No. 2017YFE0107900), the Project of Introducing Talents of Discipline Innovation to Universities 2.0 (the 111 Project of China 2.0, No. BP0719037) and China Scholarship Council (No. 201706080074). The SIMAP laboratory acknowledges the financial support provided by the ESA-MAP MICAST project contract 14347/01/NL/SH.

NOMENCLATURE

c_i	intrinsic solute concentration within i phase (wt.%)
c_{mix}	mix solute concentration (wt.%)
c_{eut}	eutectic concentration (wt.%)
$c_l^*,\ c_s^*$	equilibrium concentration at f-s and d-s interface (wt.%)
c_{env}	concentration at l-d interface (wt.%)
c_p^i	specific heat for i-phase (J $\text{kg}^{-1}\text{K}^{-1}$)
c_0	initial concentration (wt.%)
d_e	grain diameter (m)
D_l	diffusion coefficient in liquid ($\text{m}^2\ \text{s}^{-1}$)
ε	dissipation of turbulent energy ($\text{m}^2\ \text{s}^{-2}$)
f_{i}	volume fraction of i- phase (1)
$f_{e,p}$	grain packing limit (1)
h_i	Enthalpy of i- phase (J kg^{-1})
J_{ij}	Species transfer rate from i- phase to j- phase (m s^{-1})
k	solute partition coefficient (1)
k_ε	turbulent kinetic energy $\text{m}^2\ \text{s}^{-2}$
κ_i	thermal conductivity for i-phase (W $\text{m}^{-1}\text{K}^{-1}$)
K_{ij}	liquid-equiaxed drag coefficient (kg $\text{m}^{-3}\text{s}^{-1}$)
l_i	Diffusion length of i- phase (m)
L	latent heat (J kg^{-1})
M_{ij}	mass transfer rate from i- phase to j- phase
n_{max}	maximum equiaxed grain density (m^{-3})
n	grain number density (m^{-3})
N_ϕ	nuclei production rate ($\text{m}^{-3}\text{s}^{-1}$)
Re	Reynolds number
t	time(s)
T_i	temperature (K) of i phase
T_{eut}	eutectic temperature (K)
ΔT	undercooling (K)

ΔT_{nucl}	nucleation temperature (K)
$\mathbf{u}_i$	velocity vector of i- phase (m s^{-1})
v_{env}	envelope growth velocity (m s^{-1})
v_{ds}	d-s interface growth velocity (m s^{-1})
β_T	thermal expansion coefficient(K^{-1})
β_c	solutal expansion coefficient (1)
ϕ_{J}, ϕ_M	shape factor (1)
Γ	Gibbs-Thomson coefficient (m K)
λ_2	secondary arm spacing (m)
μ_i	viscosity of i- phase (kg $m^{-1}s^{-1}$)
ρ_i	density of i- phase (kg m^{-3})
ρ_{ref}	reference density (kg m^{-3})
Subscripts	
d	interdendritic melt
e: d+s	equiaxed grain phase
f: l+d	fluid phase
l	extradendritic melt
s	solid phase

Appendix A. Functions and constant used for the turbulent model

Closure relations used for solution of turbulent equations (19)-(20) are those proposed in ANSYS FLUENT for the realizable $k_\varepsilon - \varepsilon$ model and are given below in the table A.4.

Table A.4: Empirical Constants and Functions in realizable $k_\varepsilon - \varepsilon$ model

Parameters	**Parameters**
$G_{k,m} = 2\mu_t S^2$	$S = \sqrt{S_{ij}S_{ij}}$
$S_{ij} = 1/2\,(\partial u_j/\partial x_i + \partial u_i/\partial x_j)$	$C_1 = \max[0.43, \eta/(\eta+5)]$
$\eta = \sqrt{2}Sk_\varepsilon/\varepsilon$	$C_\mu = 1/(4.04 + A_s k_\varepsilon U^*)/\varepsilon)$
$A_s = \sqrt{6}\cos\varphi$	$\varphi = \cos^{-1}(\sqrt{6}W)/3$
$U^* = \sqrt{S_{ij}S_{ij} + \widetilde{\Omega}_{ij}\widetilde{\Omega}_{ij}}$	$\Omega_{ij} = 1/2\,(\partial u_j/\partial x_i - \partial u_i/\partial x_j)$
$W = S_{ij}S_{jk}S_{ki}/S^3$	$Pr_t = 0.85$
$C_2 = 1.9$	$A_0 = 4.4$
$\sigma_k = 1.0$	$\sigma_\varepsilon = 1.2$

References

[1] M. Wu, L. Könözsy, A. Ludwig, W. Schützenhöfer, R. Tanzer, On the formation of macrosegregations in steel ingot castings, Steel Res. Int. 79 (8) (2008) 637–644.

[2] D. J. Hebditch, J. D. Hunt, Observations of Ingot Macrosegregation on Model Systems., Metall. Trans. 5 (7) (1974) 1557–1564.

[3] K.-H. Spitzer, G. Reiter, K. Schwerdtfeger, Multi-frequency electromagnetic stirring of liquid metals, ISIJ Int. 36 (5) (1996) 487–492.

[4] M. Medina, Y. Du Terrail, F. Durand, Y. Fautrelle, Channel segregation during solidification and the effects of an alternating traveling magnetic field, Metall. Mater. Trans. B 35 (4) (2004) 743–754.

[5] K. S. Oh, Y. W. Chang, Macrosegregation behavior in continuously cast high carbon steel blooms and billets at the final stage of solidification in combination stirring, ISIJ Int. 35 (7) (1995) 866–875.

[6] D. Jiang, W. Wang, S. Luo, C. Ji, M. Zhu, Numerical simulation of slab centerline segregation with mechanical reduction during continuous casting process, Int. J. Heat Mass Transf. 122 (2018) 315–323.

[7] L. B. Trindade, J. E. A. Nadalon, A. C. Contini, R. C. Barroso, Modeling of solidification in continuous casting round billet with mold electromagnetic stirring (m-ems), Steel Res. Int. 88 (4) (2017) 1600319.

[8] G. Lesoult, Macrosegregation in steel strands and ingots: Characterisation, formation and consequences, Mater. Sci. Eng. A 413-414 (2005) 19 – 29.

[9] F. Wang, E. Wang, L. Zhang, P. Jia, T. Wang, Influence of electromagnetic stirring (ems) on the microstructure and mechanical property of incoloy825 superalloy, J. Manuf. Process. 26 (2017) 364 – 371.

[10] Y. Xu, T. Wang, F. Wang, E. Wang, Influence of lower frequency electromagnetic field on dendritic crystal growth in special alloys, J. Cryst. Growth 468 (2017) 506 – 509.

[11] Y. Yin, J. Zhang, S. Lei, Q. Dong, Numerical study on the capture of large inclusion in slab continuous casting with the effect of in-mold electromagnetic stirring, ISIJ Int. 57 (12) (2017) 2165–2174.

[12] Z. Yan, W. Jin, T. Li, Effect of rotating magnetic field (rmf) on segregation of solute elements in cuni10fe1mn alloy hollow billet, J. Mater. Eng. Perform. 21 (9) (2012) 1970–1977.

[13] S. Steinbach, L. Ratke, The effect of rotating magnetic fields on the microstructure of directionally solidified al-si-mg alloys, Mater. Sci. Eng. A 413-414 (2005) 200–204.

[14] O. Budenkova, A. Noeppel, J. Kovács, A. Rónaföldi, A. Roósz, A. M. Bianchi, F. Baltaretu, M. Medina, Y. Fautrelle, Comparison between simulation and experimental results of the effect of rmf on directional solidification of al-7wt.Gravity V, Vol. 649 of Mater. Sci. Forum, Trans Tech Publications Ltd, 2010, pp. 269–274.

[15] N. Shevchenko, S. Boden, G. Gerbeth, S. Eckert, Chimney formation in solidifying ga-25wt pct in alloys under the influence of thermosolutal melt convection, Metall. Mater. Trans. A 44 (8) (2013) 3797–3808.

[16] D. Jiang, M. Zhu, Center segregation with final electromagnetic stirring in billet continuous casting process, Metall. Mater. Trans. B 48 (1) (2017) 444–455.

[17] M. R. Bridge, G. D. Rogers, Structural effects and band segregate formation during the electromagnetic stirring of strand-cast steel, Metall. Trans. B 15 (3) (1984) 581–589.

[18] Q. Fang, H. Ni, B. Wang, H. Zhang, F. Ye, Effects of ems induced flow on solidification and solute transport in bloom mold, Metals 7 (3) (2017) 72.

[19] K. Dou, Z. Yang, Q. Liu, Y. Huang, H. Dong, Influence of secondary cooling mode on solidification structure and macro-segregation behavior for high-carbon continuous casting bloom, High Temp. Mater. Process. 36 (7) (2017) 741–753.

[20] S. Chen, G. Guillemot, C.-A. Gandin, 3d coupled cellular automaton (ca)finite element (fe) modeling for solidification grain structures in gas tungsten arc welding (gtaw), ISIJ Int. 54 (2) (2014) 401–407.

[21] D. A. Drew, Mathematical modeling of two-phase flow, Annu. Rev. Fluid Mech. 15 (1) (1983) 261–291.

[22] A. I. Ciobanas, Y. Fautrelle, Ensemble averaged multiphase eulerian model for columnar/equiaxed solidification of a binary alloy: I. the mathematical model, Journal of Physics D: Applied Physics 40 (12) (2007) 3733–3762.

[23] A. I. Ciobanas, Y. Fautrelle, Ensemble averaged multi-phase eulerian model for columnar/equiaxed solidification of a binary alloy: Ii. simulation of the columnar-to-equiaxed transition (cet), Journal of Physics D: Applied Physics 40 (14) (2007) 4310–4336.

[24] L. Ratke, S. Steinbach, G. Müller, M. Hainke, A. Roósz, Y. Fautrelle, M. Dupouy, G. Zimmermann, A. Weiß, H.-J. Diepers, J. Lacaze, R. Valdes, G. Grün, H.-P. Nicolai, H. Gerke-Cantow, Microstructure formation in casting of technical alloys under diffusive and magnetically controlled convective conditions, in: Solidification and Gravity IV, Vol. 508 of Mater. Sci. Forum, Trans Tech Publications Ltd, 2006, pp. 131–144.

[25] X. Wang, Y. Fautrelle, An investigation of the influence of natural convection on tin solidification using a quasi two-dimensional experimental benchmark, Int. J. Heat Mass Transf. 52 (23) (2009) 5624 – 5633.

[26] L. Hachani, K. Zaidat, B. Saadi, X. Wang, Y. Fautrelle, Solidification of snpb: Experiments on the influence of the initial concentration, Int. J. Therm. Sci. 91 (2015) 34 – 48.

[27] R. Boussaa, L. Hachani, O. Budenkova, V. Botton, D. Henry, K. Zaidat, H. B. Hadid, Y. Fautrelle, Macrosegregations in sn-3wt % pb alloy solidification: Experimental and 3d numerical simulation investigations, Int. J. Heat Mass Transf. 100 (2016) 680 – 690.

[28] Y. Zheng, M. Wu, E. Karimi-Sibaki, A. Kharicha, A. Ludwig, Use of a mixed columnar-equiaxed solidification model to analyse the formation of as-cast structure and macrosegregation in a sn-10wt% pb benchmark experiment, Int. J. Heat Mass Transf. 122 (2018) 939 – 953.

[29] T. Carozzani, C.-A. Gandin, H. Digonnet, M. Bellet, K. Zaidat, Y. Fautrelle, Direct Simulation of a Solidification Benchmark Experiment, Metall. Mater. Trans. A 44 (2) (2013) 873–887.

[30] L. Hachani, K. Zaidat, Y. Fautrelle, Experimental study of the solidification of sn-10wt.%pb alloy under different forced convection in benchmark experiment, Int. J. Heat Mass Transf. 85 (2015) 438 – 454.

[31] L. Hachani, Study of the influence of natural and forced convection on the solidification of a binary metal alloy, Phd thesis, Université de Grenoble (2013).

[32] T. Wang, S. Semenov, E. Wang, Y. Delannoy, Y. Fautrelle, O. Budenkova, Effect of diffusion length in modeling of equiaxed dendritic solidification under buoyancy flow in a configuration of Hebditch–Hunt experiment, Metall. Mater. Trans. B 50 (6) (2019) 3039–3054.

[33] X. D. Wang, P. Petitpas, C. Garnier, J.-P. Paulin, Y. Fautrelle, A quasi two-dimensional benchmark experiment for the solidification of a tin–lead binary alloy, C. R. Mec. 335 (5) (2007) 336 – 341.

[34] X. Wang, R. Moreau, J. Etay, Y. Fautrelle, A periodically reversed flow driven by a modulated traveling magnetic field: Part ii. theoretical model, Metall. Mater. Trans. B 40 (1) (2009) 104–113.

[35] M. Založnik, A. Kumar, H. Combeau, An operator splitting scheme for coupling macroscopic transport and grain growth in a two-phase multiscale solidification model: Part II– Application of the model, Comput. Mater. Sci. 48 (1) (2010) 11–21.

[36] S. V. Stankus, R. A. Khairulin, The density of alloys of tin—lead system in the solid and liquid states, High Temperature 44 (3) (2006) 389–395.

[37] Y. Plevachuk, V. Sklyarchuk, A. Yakymovych, B. Willers, S. Eckert, Electronic properties and viscosity of liquid Pb-Sn alloys, J. Alloy. Compd. 394 (1-2) (2005) 63–68.

[38] M. Wu, A. Ludwig, Modeling equiaxed solidification with melt convection and grain sedimentation–I: Model description, Acta Mater. 57 (19) (2009) 5621–5631.

[39] M. Wu, A. Ludwig, Modeling equiaxed solidification with melt convection and grain sedimentation–II. Model verification, Acta Materialia 57 (19) (2009) 5632–5644.

[40] J. Happel, Viscous flow in multiparticle systems: Slow motion of fluids relative to beds of spherical particles, AIChE Journal 4 (2) (1958) 197–201.

[41] J. Ni, C. Beckermann, A volume-averaged two-phase model for transport phenomena during solidification, Metallurgical Transactions B 22 (3) (1991) 349.

[42] A. Ludwig, M. Wu, Modeling of globular equiaxed solidification with a two-phase approach, Metall. Mater. Trans. A 33 (12) (2002) 3673–3683.

[43] A. Badillo, D. Ceynar, C. Beckermann, Growth of equiaxed dendritic crystals settling in an undercooled melt, part 2: Internal solid fraction, J. Cryst. Growth 309 (2) (2007) 216–224.

[44] J. Ni, C. Beckermann, Modeling of globulitic alloy solidification with convection, J. Mater. Process. & Manufact. Science 2 (1993) 217–231.

[45] 16.0 ANSYS Fluent User's Guide, ANSYS Inc (2015).

[46] P. Prescott, F. Incropera, The effect of turbulence on solidification of a binary metal alloy with electromagnetic stirring, J. Heat Transf. 117 (3) (1995) 716–724.

[47] W. Shyy, Y. Pang, G. B. Hunter, D. Y. Wei, M.-H. Chen, Effect of turbulent heat transfer on continuous ingot solidification, J. Eng. Mater. Technol. 115 (1) (1993) 8–16.

[48] G. M. Poole, M. Heyen, L. Nastac, N. El-Kaddah, Numerical modeling of macrosegregation in binary alloys solidifying in the presence of electromagnetic stirring, Metall. Mater. Trans. B 45 (5) (2014) 1834–1841.

[49] S. Sachi, M. Založnik, H. Combeau, C.-A. Gandin, M. Gennesson, J. Demurger, M. Stoltz, I. Poitrault, Analysis of columnar-to-equiaxed transition experiment in lab scale steel casting by a multiphase model, in: IOP Conference Series: Materials Science and Engineering, Vol. 529, IOP Publishing, 2019, p. 012039.